Advanced Composites and Hybrid Materials (2025) 8:392
https://doi.org/10.1007/s42114-025-01418-7

RESEARCH

A straightforward route to hexagonal-boron nitride fibers

Ping-Yuan Lee[1] · Barbara M. Maciejewska[1] · Mathew J. Cross[2] · Chloe M. van Beek[2] · Claire N. Brodie[2] · Athul S. Bhaskaran[4] · George T. Tebbutt[1] · Ryan M. Schofield[1] · Samuel J. Page[3] · Ed Darnbrough[1] · Marcel Swart[4,5] · Andrew S. Weller[2] · Nicole Grobert[1]

Received: 20 June 2025 / Revised: 29 July 2025 / Accepted: 7 August 2025

Abstract

Advanced fibers enable the fabrication of structures and composites for applications reliant on lightweight, oxidation resistant, mechanically strong, and electrically insulating materials, *e.g.* in all forms of land, air, and space transportation and in applications within extreme environments. Hexagonal boron nitride (h-BN) fibers harness these advantages, and in addition, offer ultra-high-strength-to-weight ratio and low density. Yet, existing precursors for polymer-derived BN fibers are limited to insoluble and air/moisture sensitive polyborazylenes, hindering fiber production at scale. In this contribution, we report a reliable, controllable, and scalable synthesis methodology for producing pure micro- and nano-h-BN fibers, offering a competitive alternative to NASA's energy-intensive h-BN nanotubes production. The single-source precursor, *N*-methyl polyaminoborane (PMeAB), plays a pivotal role in this process. The catalytic, and scalable, synthesis of PMeAB with controlled molecular weights (M_w = 110,500–290,500 g·mol^{-1}) enables the production of h-BN fibers by electrospinning method and thermolysis under ammonia. PMeAB molecular weight and concentration were identified as key factors dictating the viscosity and surface tension, and thus influencing the overall spinnability of the PMeAB solution. We reveal that the subsequent formation of a cross-linked intermediate during PMeAB thermolysis is essential to retain the fibrous morphology during the conversion to h-BN fibers. Comprehensive characterization demonstrated the purity and homogeneity of the h-BN fibers, with ~ 97 at.% of B and N contents combined throughout the fiber body. This newly disclosed route to h-BN fibers offers a route to potentially valuable multifunctional filler material for advanced lightweight composites suitable for applications in extreme environments.

Keywords Polymer-derived h-BN fibres · Manufacturing · Electrospinning · Thermolysis · High-molecular weight PMeAB

1 Introduction

Pure hexagonal boron nitride (h-BN) fibers are sought after for ultra-lightweight applications that need to perform in extreme environments, *e.g.*, those typically found in space, aerospace, and other means of transportation [1–3]. Hexagonal boron nitride fibers are particularly interesting due to their isoelectronic relationship with, and closely related structures to, carbon-based materials. h-BN fibers present certain advantages over carbon fiber counterparts. Compared with carbon fibers, h-BN fibers are electrically insulating [4] and have superior thermal stability and chemical inertness [5–8]. These properties, coupled with high Young's modulus of fibrous BN, make h-BN fibers potentially the strongest known insulating material to date [8]. h-BN fibers also possess the exceptionally rare combination of being both a dielectric and a thermal conductor [9]. They outperform carbon fibers in thermal stability in both oxidizing and inert atmospheres and exhibit much greater

✉ Barbara M. Maciejewska
barbara.maciejewska@materials.ox.ac.uk

✉ Andrew S. Weller
andrew.weller@york.ac.uk

✉ Nicole Grobert
nicole.grobert@materials.ox.ac.uk

[1] Department of Materials, University of Oxford, Parks Road, Oxford OX1 3PH, UK

[2] Department of Chemistry, University of York, Heslington, York YO10 5DD, UK

[3] Department of Chemistry, University of Durham, Durham DH1 3LE, UK

[4] IQCC and Department of Chemistry, University of Girona, Girona 17003, Spain

[5] ICREA, Barcelona 08010, Spain

Published online: 08 October 2025

chemical resistance to extreme conditions [10]. Despite these outstanding properties, and existing demand, the availability of h-BN fibers is limited as current synthetic routes are not straightforward. Therefore, only few reports on the synthesis of h-BN fibers exist to date. Among the key bottlenecks are the properties of BN precursor systems and their subsequent processability into fibers [11–13]. Of those systems reported, the fiber sizes, crystalline structures, corresponding morphologies, and the overall quality—including purity, crystallinity, porosity, homogeneity—of h-BN fibers, have varied widely, and progress towards their potential for reliable accessible and scalable manufacturing has been limited [10, 12, 14–18].

In the past decade, NASA reported the synthesis of small–diameter BN nanotubes; however, the process requires specialized high-power lasers and operates at high pressures and temperatures, limiting their wider use [19]. Chemical vapor deposition and template methods have also been explored for BN nanotube synthesis, although these approaches similarly face challenges in scalability for fiber production [20]. More recently, to produce BN fibers, NASA introduced force-spinning using carbon-rich polymers to make the solution spinnable. However, the carbon content was too high for BN fibers to form [21, 22]. The method for h-BN fibers synthesis has centered around melt-spinning, hot extrusion, and electrospinning of boron-oxide-containing polymer precursors followed by themolysis [11]. Precursors employed in these studies were either polymer additive-aided colloidal particles or polyborazylene-based single-source polymer ceramic precursors. For example, by electrospinning B_2O_3/PVB-additive mixtures followed by high temperature nitridation, Qiu et al. [15, 16] produced long, aligned, BN nanofibers (*ca.* 100 nm in diameter and *ca*. 13 cm in length), which had a porous structure due to uneven solid vapor nitridation and were also produced in low ceramic yield (< 20 wt.%). Polymer-derived ceramic routes that use melt spinning processes offer precise control over precursor compositions [17], because polyborazylene precursors already contain units of hexagonal B–N rings, leading to very high reported ceramic yields (90 wt.%) [12]. However, polyborazylene is air-sensitive [23–28], has low solubility in common solvents, precluding electrospinning, and requires specially designed polymer melt processing equipment and strict operation conditions [24–26]. Moreover, it presents a challenging synthesis from borazine that is not readily deployable [29–31].

Electrospinning of a suitable BN-polymeric material would provide a straightforward and efficient way to create continuous polymer and ceramic fibers with diameters ranging from micro- to nanoscale [32, 33]. For the generation of high-quality BN fibers using this approach, the design of suitable precursors that are stable and can be dissolved in common solvents is critical [34]. One such potential precursor is the main-group polymer [35], *N*-methylpolyaminoborane, $[(H_2BNMeH)_n]$ (PMeAB), which is best prepared by catalytic routes [36, 37], (although stoichiometric methods are also known [38, 39]) as first reported by Manners in 2008, using the catalyst Ir(^{t}Bu-POCOP)H_2**[Ir]** (^{t}Bu-POCOP = κ^3-(OP^{t}Bu$_2$)$_2$C$_6$H$_3$) [40, 41]. With this catalyst (at 0.3 mol% loadings) the commercially available amine-borane pre-monomer, $H_3B{\cdot}NMeH_2$ (MeAB), was reported to undergo an atom-efficient dehydropolymerization to form PMeAB, where H_2 is the only co-product (M_w = 160,000 g·mol^{-1}, $Đ$ = 2.9) [40–42].

PMeAB is a promising precursor for the manufacture of BN fibers by electrospinning methods because of its: (i) 58% of B–N content, (ii) good solubility in common solvents such as THF or $CHCl_3$, and (iii) its stability at room temperature as an easy-to-handle solid. However, the electrospinning and subsequent thermolysis of PMeAB have not been reported in any detail [40, 43], and the optimal parameters for these processes with regard to polymer chain length have yet to be determined. This is because methods to precisely control polymer chain length (and thus optimal spinning characteristics) over a wide M_w range using robust and reliable catalysts have not been developed. There have, however, been sporadic reports on the use of powdered polyaminoboranes as potential pre-ceramics to BN. The thermolysis of parent, powdered and insoluble, $[H_2BNH_2]_n$ was reported by Kim and co-workers [44], while Manners and co-workers reported thermolysis of pelletized PMeAB [40]. The pyrolysis of MeAB [45] has been reported to form an ill-defined cross-linked solid. To our knowledge, there have been no reports on the use of PMeAB to generate h-BN fibers.

The Weller group has recently demonstrated that partial control [46] over the degree of polymerization (M_w) in PMeAB synthesis can be achieved using the air-tolerant pre-catalyst [Rh(L)(NBD)]Cl, **[Rh]**, [L = κ^3-(^{i}Pr$_2$PCH$_2$CH$_2$)$_2$NH, NBD = norbornadiene], and a boronium chain-control agent, that reduces the M_w from 133,100 g·mol^{-1} to, for example, 64,400 g·mol^{-1} ($Đ$ = 1.7) in a controlled manner [47]. This readily assembled, air-stable, pre-catalyst **[Rh]** can also be used at very low catalyst loadings (0.01 mol%) to produce PMeAB on a 10 g scale, opening the field to scalable, cost effective routes to PMeAB. However, methods to precisely tune PMeAB M_w in a systematic, controlled, and experimentally robust manner to give higher M_w above ~ 160,000 g·mol^{-1}, on a scale suitable for potential exploitation in BN fiber manufacture, that also use low catalyst loadings (i.e. 0.1 mol% or lower), have not been reported [48].

In this contribution, we now describe the development of a new polymer-derived ceramic route to BN fibers using PMeAB (Fig. 1a). This approach uses a potentially scalable and straightforward polymer pre-ceramic synthesis of PMeAB, with low loadings of catalyst to offer fine control of the polymer over a wide range of M_w (Fig. 1b, c). Subsequent additive-free electrospinning of polymer samples

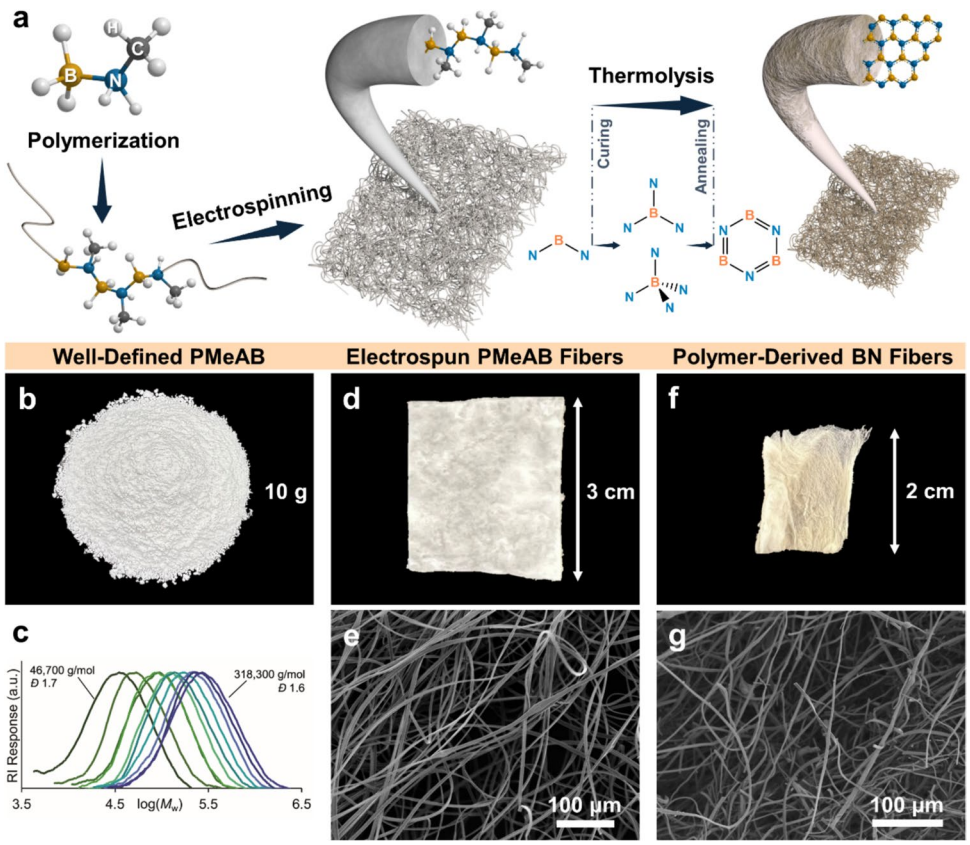

Fig. 1 **a** Schematic synthetic route toward PMeAB fibers and BN fibers. **b** As-synthesized PMeAB powder. **c** Overlaid GPC traces of the PMeAB prepared as shown in Fig. 2c. **d** PMeAB fibers and **f** BN fibers. Typical SEM images for **e** PMeAB fibers and **g** BN fibers

with optimal M_w (Fig. 1d, e), curing (cross-linking), and thermolysis yields ultra-high purity micro- and nanoscale BN fibers (Fig. 1f, g). Detailed characterization provides composition, phase, microstructure, and morphology characteristics of these BN fibers. Our results offer a straightforward method for producing high-quality BN fibers from commercially available starting materials, as well as fundamental, underpinning observations that serve as a basis for the further design of other BN-containing structures.

2 Results and discussion

2.1 Controlled catalytic synthesis of *N*-methyl poly(aminoborane) between M_w = 46,700 and 318,300 g·mol^{-1}

PMeAB is formed by a cascade-like dehydropolymierzation [49], in which the catalyst first dehydrogenates $H_3B{\cdot}NMeH_2$ to form the aminoborane, $H_2B=NMeH$ (Fig. 2a). This highly reactive species [50] then undergoes a rapid low-barrier nucleophilic head-to-tail chain-growth polymerization via the amido-end group of the growing polymer chain, with propagation likely initiated by a metal hydride or free amine [51]. For classical chain-growth polymerizations, the degree of polymerization (D.P.) will be determined by the relative rates of propagation versus termination, i.e. D.P. $\propto R_{(prop)}/R_{(term)}$ [52]. While the chain-control/termination events are not fully resolved in amine-borane dehydropolymerization, termination by quenching of the reactive amido end group by Lewis-acidic "BH_3" is a plausible mechanistic scenario, with the "BH_3" produced by endergonic dissociation of $H_3B{\cdot}NMeH_2$ [53]. Other chain control events have been proposed, including a related quenching of the amido end group by ammonium $[NH_4]^+$ or boronium $[H_2B(NMeH)_2]^+$, the latter leading to chain transfer [47]. Collectively, these processes lead to a polymer being isolated with shorter polymer chain lengths.

In order to control the degree of polymerization, and especially to access longer polymer chain lengths, we targeted approaches to control termination, and combined these with different catalyst systems (**[Ir]** [54], **[Rh]** [47], and **[Ru]** [55, 56]) (Fig. 2b), to establish a set of catalysts/conditions that holistically provide a continuum of different PMeAB chain lengths. This approach allowed for the empirical iterative development of a set of conditions that led to the isolation of PMeAB with a wide range of M_w: ranging from 46,700 g·mol^{-1} to 318,300 g·mol^{-1} ($Đ$ = 1.5–1.7), in ~ 40,000 g·mol^{-1} steps, **PMeAB1** to **PMeAB10** (Fig. 2c). In all cases, 100% conversion of starting material was

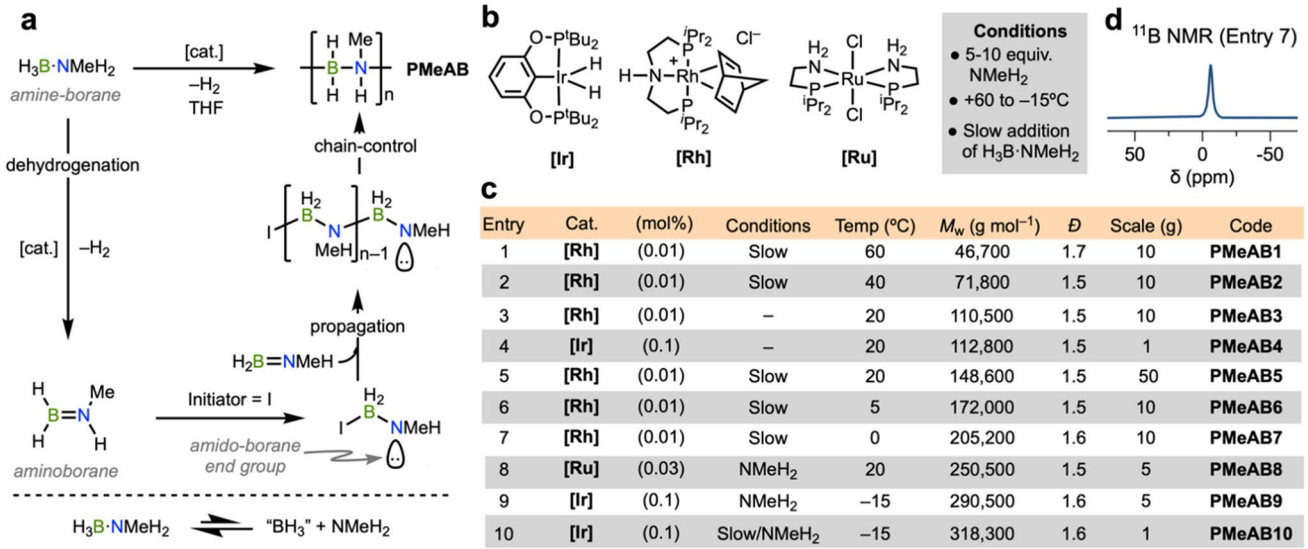

c

Entry	Cat.	(mol%)	Conditions	Temp (°C)	M_w (g mol^{-1})	$Đ$	Scale (g)	Code
1	**[Rh]**	(0.01)	Slow	60	46,700	1.7	10	**PMeAB1**
2	**[Rh]**	(0.01)	Slow	40	71,800	1.5	10	**PMeAB2**
3	**[Rh]**	(0.01)	–	20	110,500	1.5	10	**PMeAB3**
4	**[Ir]**	(0.1)	–	20	112,800	1.5	1	**PMeAB4**
5	**[Rh]**	(0.01)	Slow	20	148,600	1.5	50	**PMeAB5**
6	**[Rh]**	(0.01)	Slow	5	172,000	1.5	10	**PMeAB6**
7	**[Rh]**	(0.01)	Slow	0	205,200	1.6	10	**PMeAB7**
8	**[Ru]**	(0.03)	$NMeH_2$	20	250,500	1.5	5	**PMeAB8**
9	**[Ir]**	(0.1)	$NMeH_2$	–15	290,500	1.6	5	**PMeAB9**
10	**[Ir]**	(0.1)	Slow/$NMeH_2$	–15	318,300	1.6	1	**PMeAB10**

Fig. 2 **a** Amine borane-dehydropolymerization and dissociation of $H_3B{\cdot}NMeH_2$. **b** Precatalysts and variation of conditions. $[H_3B{\cdot}NMeH_2] = 1–5$ M. **c** Dehydropolymerization conditions and details of resulting polymers (see Supporting Materials for full experimental conditions). **d** ^{11}B NMR spectrum of PMeAB ($CDCl_3$, Entry 7, $M_w = 205{,}200$ g·mol^{-1})

observed, with > 99% selectivity for mono-modal PMeAB, as measured by ^{11}B NMR spectroscopy and gel permeation chromatography (GPC). To detail our approach:

(i) Slow dropwise addition of $H_3B{\cdot}NMeH_2$ to the reaction solution (0.1 cm^3·min^{-1}) results in increased M_w (*cf.* entries 3 and 5 at 20 °C). Under the previously noted reaction kinetics of zero-order in substrate for pre-catalyst **[Rh]**[47] that are also established here for **[Ir]** (Figure S1), such dropwise addition would not be expected to affect the rate of catalyst turnover (*i.e.*, propagation) but would keep excess $H_3B{\cdot}NMeH_2$, and thus free "BH_3," a potential chain-terminating agent, to a minimum.

(ii) Variation of the reaction temperatures (ranging from 60 °C to – 15 °C) results in increasingly higher degrees of polymerization with lower temperatures (*cf.* entries 1, 2, 6, 7). This is an observation consistent with classical anionic- or cationic chain-growth polymerizations where there is often a higher barrier to termination compared with propagation, and thus lower temperatures favor the latter [52]. Lower temperatures would also be expected to bias the endergonic dissociative equilibrium of $H_3B{\cdot}NMeH_2$ in THF to disfavor the formation of "BH_3" [53].

(iii) Addition of 5 equivalents of $NMeH_2$ results in higher degrees of polymerization, consistent with its role in sequestering free "BH_3." This amine also likely attenuates the formation of dormant borohydride complexes [57] and promotes pre-catalyst initiation/productive turnover [36]. This method can also be combined with low temperatures and slow addition of $H_3B{\cdot}NMeH_2$ to generate the very highest degrees of polymerization (entries 8–10).

(iv) To demonstrate wide applicability, commercially available Ir(^{t}Bu-POCOP)HCl can also be used as an effective pre-catalyst at 0.1 mol% to selectively produce PMeAB of M_w 219,000 g·mol^{-1} ($Đ = 1.5$), which is in the range suitable for spinnable fibers, vide infra (see Supporting Materials).

Selectively-synthesized PMeAB were isolated as white, air-stable solids after precipitation into pentane (Fig. 1b), with good isolated yields (64–92%). The **PMeAB** was stable on the bench under ambient conditions as a solid for over 1 year, as measured by ^{11}B NMR spectroscopy (Supporting Materials). Solutions in wet solvent (*i.e.*, 300 ppm water in THF) undergo partial hydrolysis over 7 days to form boric acid. In the solution ^{11}B NMR spectra of these polymers ($CDCl_3$) a characteristic single broad resonance for $[H_2BNMeH_2]_n$ is observed at $\delta \sim -6$ ppm (Fig. 2d) [40]. Analysis by GPC (relative to polystyrene standards) showed monomodal distributions for all polymer samples (Fig. 1c). As well as control of polymer chain length, these experiments show that low catalyst loadings (0.01 mol%) and concentrated (1–5M) THF solutions of $H_3B{\cdot}NMeH_2$ can be used, leading to further efficiencies in synthesis. While the catalyst is used at low loadings (*e.g.*, 0.01 mol%) it remains entrained in the isolated polymer, as measured by ICP-OES (Inductively Coupled Plasma Optical Emission Spectroscopy, e.g. **PMeAB7**, 183 ppm w/w). Using the

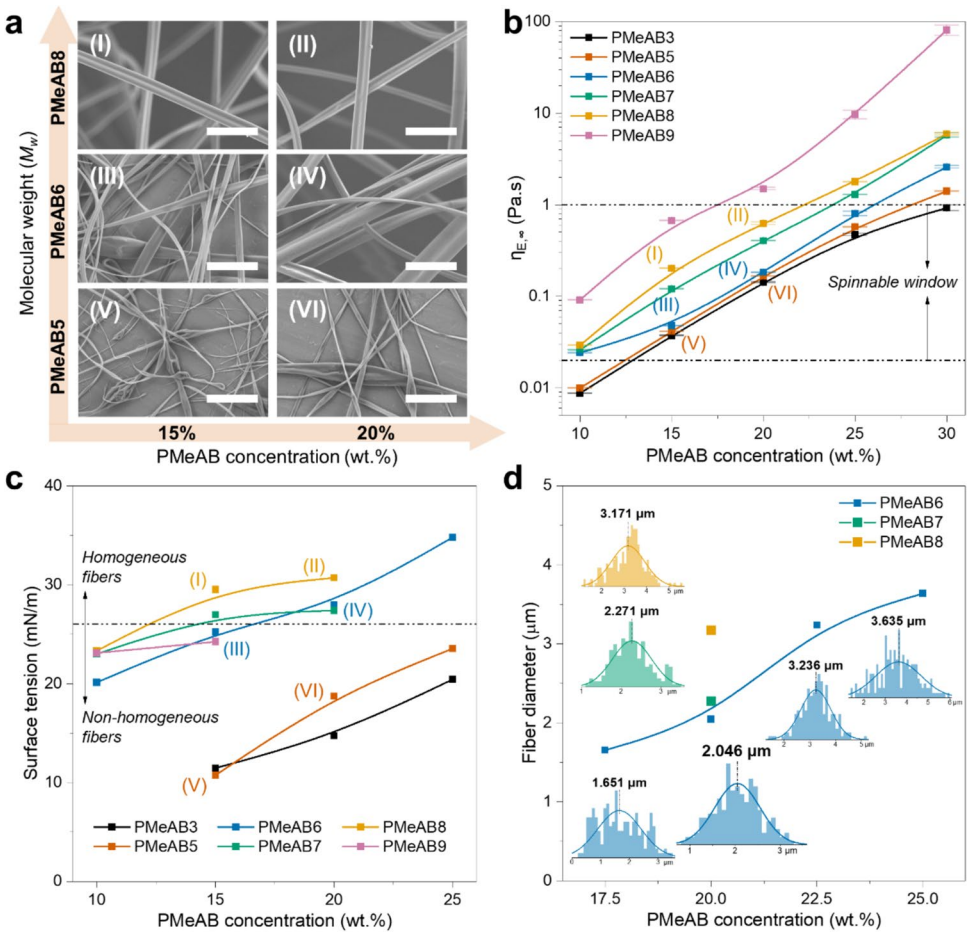

Fig. 3 **a** Morphology of the electrospun PMeABF using representative PMeAB M_w and concentrations. (universal scale bar: 5 μm). **b** Viscosity effects on the spinnability of PMeAB solutions. **c** Surface tension effects on the diameter distribution of the electrospun PMeABF. **d** Polymer concentration and M_w effects on the diameter of the electrospun PMeABF

[Rh] pre-catalyst, scale-up to 50 g of isolated polymer has been demonstrated at 0.01 mol% catalyst loading (20 °C), Entry 5. Analysis by ^{11}B NMR spectroscopy (Supporting Materials) and GPC of the resulting polymer showed that **PMeAB5** was formed selectively in a monomodal distribution ($M_w = 148{,}600$ g·mol^{-1}, $Đ = 1.5$).[1] While this is unoptimized with regard to catalyst loading and overall Process Mass Intensity, this represents a cost of £0.14 of catalyst used per gram of polymer synthesized. These resulting polymers were then used, without further modification or processing, for electrospinning studies—as is detailed next.

2.2 Electrospinning PMeAB solutions

The key solution parameters necessary for optimal electrospinning conditions were determined using polymer samples **PMeAB1** to **PMeAB9**. The concentration of PMeAB solutions ($CHCl_3$) varied from 5 to 30 wt.%; with the spinning solutions labeled as **PMeABX-Y%**, where Y corresponds to the weight percentage of PMeAB. Figure 3 shows the key results from these studies, that demonstrate that both PMeAB molecular weight and its concentration determine spinning behavior and resulting fiber morphology. Electrospinning of PMeAB with lower M_w, i.e., **PMeAB1**, **PMeAB2**, **PMeAB3**, **PMeAB4**, **PMeAB5,** at concentrations below 10 wt.% typically resulted in the formation of droplets instead of fibers. At polymer concentrations between 15 and 30 wt.%, the solutions became spinnable. This corresponds to the overlap concentration (c*), wherein a sufficient level of polymer chain entanglement is achieved [58]. While electrospinning of **PMeAB5-15%** led to fibers with beads, Fig. 3a(V), increasing the concentration to **PMeAB5-20%** and **PMeAB5-25%** partially suppressed bead formation, *e.g.* Figure 3a(VI). Further increasing the concentration to **PMeAB5-30%** makes the solution too viscous to be electrospun. Comparing **PMeAB1, 2, 3, 4, and PMeAB5** with higher M_w PMeAB, such as **PMeAB6** and **PMeAB7**, at the same polymer concentration (20% or 25%), revealed that **PMeAB6** and

[1] The increase in M_w of polymer produced on 50 g scale compared to a 10 g scale (entry 3, Fig. 2c) is likely due to the combination of dropwise addition of $H_3B{\cdot}NMeH_2$ and mass transport considerations from using a mechanical overhead stirrer on this scale. We have found this process to be reliable and repeatable, and the polymer formed sits in the window suitable for electrospinning.

PMeAB7 form more homogeneous fibers with significantly fewer beads, see Figs. 3a(III) vs (V) and Fig. 3a(IV) vs (VI). Notably, electrospinning **PMeAB6-20%** yields fibers without any beads. The further increase of the M_w using **PMeAB8** and **PMeAB9** results in high-quality bead-free fibers, when a concentration of 15 wt.% is used, Fig. 3a(I). PMeAB with molecular weights ranging from $M_w = 110{,}500$ (**PMeAB3**) to 250,500 g·mol^{-1} (**PMeAB8**), at concentrations between 15 and 20%, were found to be optimal for electrospinning in $CHCl_3$ solvent. The very high molecular weight **PMeAB10** was not tested further.

Parametric studies, focusing on the viscosity and surface tension of the PMeAB solutions, have been used to establish optimal conditions for the electrospinning of PMeAB fibers (PMeABF). A viscosity of approximately 0.02 Pa·s is sufficient for the PMeAB solution to be spinnable (Fig. 3b). However, above a viscosity threshold of ~ 1 Pa·s, electrospinning is not possible due to the high cohesion of the solution. Within this spinnable window (0.02 to 1 Pa·s), the quality of the electrospun fibers varies. This variation is attributed to the surface tension of the spinning solution, which is influenced by its composition and directly impacts the quality of the fibers produced, and is a result of the intermolecular interactions between the polymer chains and the solvent molecules [59, 60]. As surface tension increases with an increase in polymer concentration, this allows for an assessment of the lower limit for effective electrospinning, which is shown to be 26 mN·m^{-1} (Fig. 3c). Above this limit, PMeAB solutions are reliably spinnable, generating fibers of good quality, high homogeneity, and continuity. The estimated optimal viscosity of 0.02 ~ 1 Pa·s and minimum surface tension of 26 mN·m^{-1} agree well with values reported in literature [61].

The diameter of spun-fibers is related to mechanical properties and surface area-to-volume ratio, and impacts the overall tensile strength, flexibility, and functionality of the material. Fiber diameter can be tuned by the selection of solution and/or electrospinning parameters. The electrospun PMeABF isolated here has diameters ranging from several microns to less than 100 nm. Despite a broad diameter distribution within each sample, a general trend is notable: as the concentration or molecular weight of the polymer increases, the average diameter of the fibers tends to increase (Fig. 3d). This is consistent with literature precedent for other electrospun fibers and shows that using higher concentrations or molecular weights of polymer results in thicker electrospun fibers. This is likely due to more extensive polymer chain entanglement within the spinning solution [62, 63].

There was no change to the chemical composition of PMeABF after electrospinning, as measured by solution ^{1}H and ^{11}B NMR spectroscopy (Figures S3, S17). The ^{1}H NMR spectrum for spun PMeABF also showed no residual $CHCl_3$ solvent (Figure S3).

2.3 Conversion of PMeAB fibers to BN fibers

The conversion of PMeABF to the desired h-BN fibers product requires two key steps: vacuum curing and subsequent high-temperature annealing under NH_3 (ammonolysis). One of the challenges of any conversion process is preserving the shape of the fibers (Figure S4). The methodology developed here was a sequential low-temperature vacuum curing (100 °C for 48 h) of as-spun ("raw") PMeABF followed by high-temperature annealing in an NH_3 atmosphere. As shown in Fig. 4a (and Figure S5), the surface and Cross-section of the raw PMeABF are smooth and dense, with an average fiber diameter of 3.64 µm. Following curing (Fig. 4b), the average diameter of PMeABF becomes 3.56 µm and the fiber now has a dense surface with some roughness observed at the cross-section. After annealing (Fig. 4c), the h-BN fiber retains its well-defined fibrous morphology, and the surface remains dense, without visible defects or pores (Figure S6). Crystallization is observable at the Cross-section, indicating the overall conversion from PMeAB polymer to BN ceramic. The average diameter of the h-BN fibers is 3.38 µm, which is not significantly different from PMeABF. Unlike other kinds of polymer-derived ceramics that show notable size reduction,[11] PMeAB-derived h-BN fibers exhibit only a small volume shrinkage of 7% [11]. The main difference between raw and cured PMeABF is that the latter is not soluble in solvents such as $CHCl_3$, THF, or DMF. Following this, electro-spinning and curing processes using solid-state [11] ^{11}B NMR spectroscopy showed no difference between PMeAB and precured PMeABF, Fig. 4 d, with a broad signal observed at $\delta \sim -8$, consistent with solution ^{11}B NMR spectra. In contrast, the ^{11}B solid-state NMR spectrum of the cured PMeABF shows a decrease in the intensity of this $\delta \sim -8$ signal, and new signals at $\delta \sim 10$ (broad) and $\delta \sim 1$ (sharp) are observed. The linewidths and chemical shifts of these new signals are characteristic of boron coordinated by three and four nitrogens, respectively, as previously noted for polymers derived from the dehydrocoupling of hydrazineborane [64, 65].

Computational ^{11}B NMR calculations based on density functional theory (DFT) using the KT2 functional (COSMO, ZORA, see SI for details) confirm these ^{11}B assignments by assigning the peak positions (Fig. 4e). A benchmark study was first performed that showed an almost perfectly correlated relationship between experimental NMR values and our DFT chemical shifts. With this relationship in hand, we find good correlation between the computational value and the experimental data of the relevant boron-based structures in the literature. Based on this method, the molecular structures of cured PMeABF potentially comprise of a mixture of four coordinate BN_3H, BN_4 and BN_2H. Collectively, experimental and computational results indicate the cross-linking

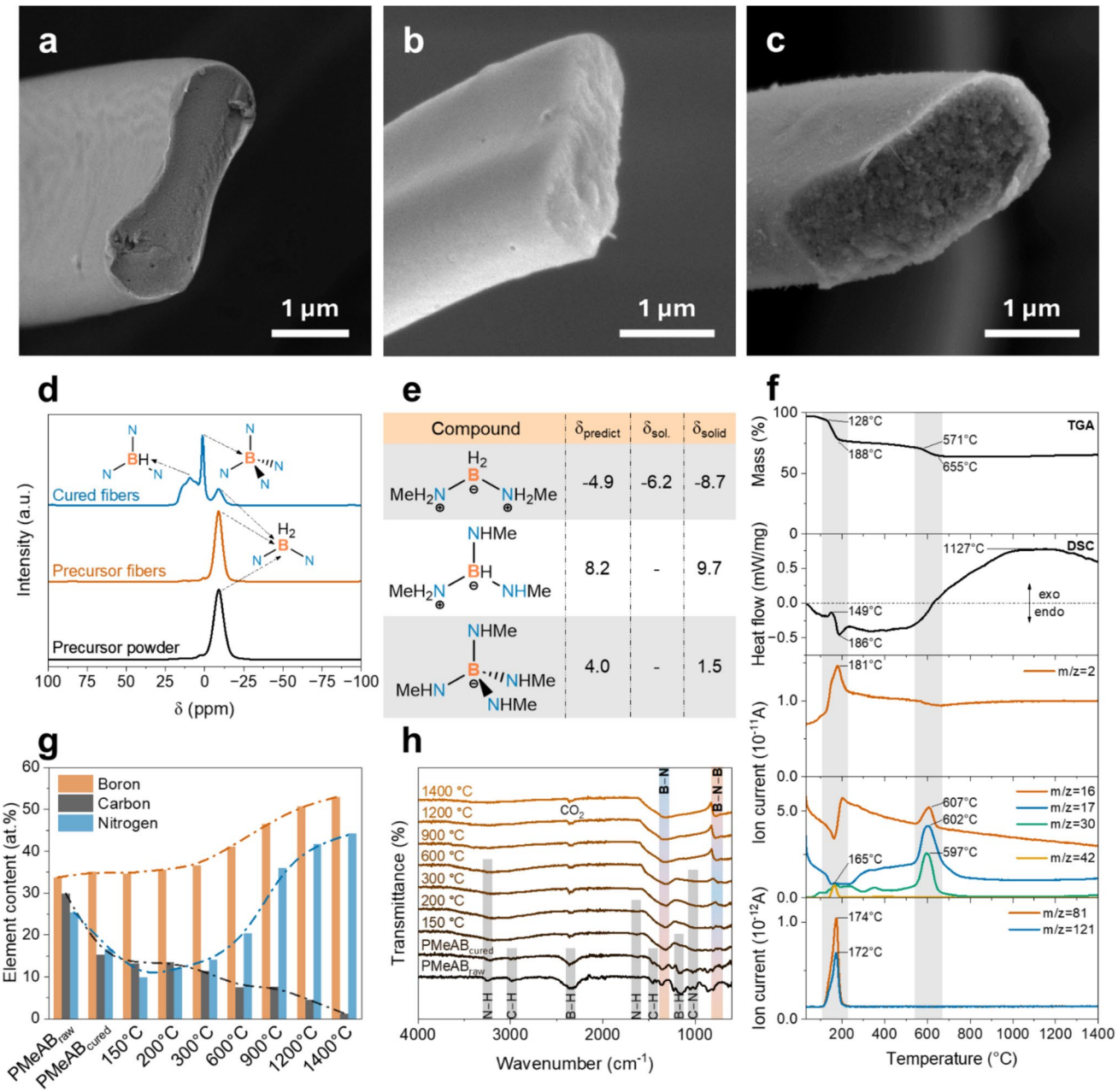

Fig. 4 **a**–**c** Typical SEM images for the cross-section of **a** a raw PMeABF, **b** a cured PMeABF, and **c** a BNF. **d** Representative solid-state ^{11}B NMR spectra of PMeABF before and after curing process. **e** Calculated NMR chemical shift values of predicted boron structures based on DFT, see SI for details. **f** Synchronous TG–MS analysis for the released products During heating of cured PMeABF up to 100 °C in Ar. **g** Element contents of PMeABF annealed at different temperatures (calculated from XPS spectra). **h** FT-IR spectra of PMeABF annealed at different temperatures

behavior toward higher BN coordination numbers, which occurred within the PMeABF during the vacuum curing process.

Figure 4f and Figure S7 show the TGA–DSC-MS spectra for both precursor and cured PMeABF samples as measured under an argon atmosphere. While these TGA–DSC-MS conditions do not replicate the actual conversion process, they give valuable information about the thermal decomposition behaviors of both cured and uncured PMeABF. The TGA of cured PMeABF showed significantly less weight loss, *i.e.*, 36.1 wt.%, During thermal decomposition, compared to 81.9 wt.% for the uncured precursor PMeABF. This limited weight loss can be explained by (i) the gradual release of volatile substances during the curing process and (ii) the formation of a stable cross-linked polymer structure in the cured PMeABF, compared to the linear polymer

structure of the precursor PMeABF. The curing process, instead of rapid decomposition reactions during annealing, enables a controlled release of substances, enhancing thermal stability of PMeABF and reducing the overall weight loss.

Comparing the corresponding MS spectra obtained from precursor and cured PMeABF shows that hydrogen, methane, ammonia, $NHCH_3$ (m/z = 30), BNH_2CH_3 (m/z = 42), borazine ($B_3N_3H_6$, m/z = 81), and tri-methyl-substituted borazine [$B_3N_3H_3(CH_3)_3$, m/z = 121] were detected for both samples During thermolysis. These compounds are significant for PMeABF, while their relative concentrations were lowered for cured PMeABF. Notably, the ceramic yield of cured PMeAB fibers is 63.9%. These observations agree those noted for polyborazlyene under TGA-MS analyses and underscore the importance of the curing step for the efficient conversion of PMeAB to BN [45]. In support of this hypothesis, when uncured PMeABF is exposed to the high-temperature annealing process in ammonia, melting and rapid release of gases occurs at relatively low temperatures above 120 °C (Figures S7, S8). This behavior has been noted to be observed for monomer MeAB of PMeAB and its close relative AB at temperatures ranging from 100 to 150 °C [45, 66].

Analysis by XPS and FT-IR allows for the evolution of the gross elemental and structural composition of PMeABF to h-BN fibers to be determined (Fig. 4 g, h). Figure 4 g shows the B, C, and N elemental content derived from the corresponding XPS spectra (Figure S9) for raw-electrospun PMeABF, cured PMeABF, and cured then annealed PMeABF at various temperatures between 150 and 1400 °C in NH_3. NH_3 is used to eliminate the carbon impurities, introduced from the methyl group in PMeAB, which is critical to achieve high-purity h-BN. Guilhon et al. studied tris(isopropylamino)borane as the precursor to synthesize BN through thermal treatment in NH_3, proposing that NH_3 facilitates the elimination process of methyl amine and CH_4 [13]. This observation aligns with our XPS results, in which the C and N contents decrease simultaneously up to 150 °C, while the N content starts to increase at 200 °C onward, with the C content diminishing significantly, to less than 2%. It is proposed that the reducing nature of the NH_3 environment not only facilitates further release of amine and CH_4 from the precursor fibers but also provides an additional N source to react with B-rich intermediates. Figure 4h shows FT-IR spectra for PMeABF, cured PMeABF, and cured PMeABF annealed at temperatures between 150 °C and 1400 °C. The spectra for cured PMeABF that has been annealed at 150 °C, 200 °C, and 300 °C show a gradual increase in intensity of B – N stretching (1320 cm^{-1}) and B – N bending (758 cm^{-1}) modes, while B – H (2342 cm^{-1}) and C – H (1456 cm^{-1} and 2984 cm^{-1}) stretching modes gradually decrease. In the temperature range between 300 °C and 900 °C, N – H and N – C stretching modes disappear due to the removal of the N – H terminal group and the C content decreases due to ammonolysis [15, 44, 66]. The spectra for cured PMeABF annealed at 900 °C and above have only the B – N stretching and B – N bending modes present [67]. The effective removal of C species from B-C-N-rich polymers during the annealing process in NH_3 has been discussed previsouly [17, 68–70]. The elemental ratio for h-BN fibers produced through annealing PMeABF at 1400 °C in NH_3 is 1:1.2, which suggests a nearly stoichiometric composition of B and N elements, with a negligible carbon impurity of 1.31%.

2.4 Detailed characterization of the BN fibers

An XPS analysis of the synthesized h-BN fibers shows B 1 s (190.4 eV), C 1 s (284.8 eV), N 1 s (398.0 eV), and O 1 s (533.1 eV) peaks confirming the intrinsic BN nature (Fig. 5d) [71]. The presence of significantly weaker signals at approximately 188.7 eV and 396.6 eV for B – C and N – C, respectively [72, 73], is consistent with less than 2% of these C impurities. B – O (~ 192.5 eV) [72] and N – O (~ 400.4 eV) [73] modes for the h-BN fibers are present in low intensity (Fig. 5a, c). The presence of minor oxygen impurities in the sample could potentially be attributed to small amounts of oxidation or moisture adsorption occurring During sample preparation under an ambient atmosphere. The atomic percentages of B and N are measured as 52.34% and 44.73%, respectively, which aligns with the B-rich composition indicated by the EDX line profile results (Fig. 5e). Elemental mapping analysis (Fig. 5e) provides evidence for the homogeneous distribution of B and N within the h-BN fibers. While we have not specifically assessed the electrical insulation and thermal conductivity properties of these BN fibers, it is reasonable to anticipate that such low impurity levels would have a minimal impact on the physical properties of the material. Studies have shown that the presence of oxygen impurities can influence the thermal conductivity of BN materials. For example, research on boron nitride nanotubes indicates that oxygen impurities, resulting from partial oxidation, can affect their thermal properties [7]. However, given the minor impurity content in our samples, any effect on the insulation and thermal conductivity is expected to be negligible.

The FT-IR spectra for both synthesized h-BN fibers and commercial exfoliated h-BN nanosheets (BNNS) were compared (Fig. 5f). For BNNS, two distinct absorption peaks are observed at 1359 and 802 cm^{-1} corresponding to in-plane B – N stretching vibration of sp^2-bonded h-BN and out-of-plane B – N – B bending vibration [74]. The h-BN fibers show two, very similar, sharp absorption peaks at 1354 and 798 cm^{-1} but the relative peak intensity for B – N to B – N – B bending vibration is higher than that for BNNS. This is most likely due to the larger thickness of h-BN fibers

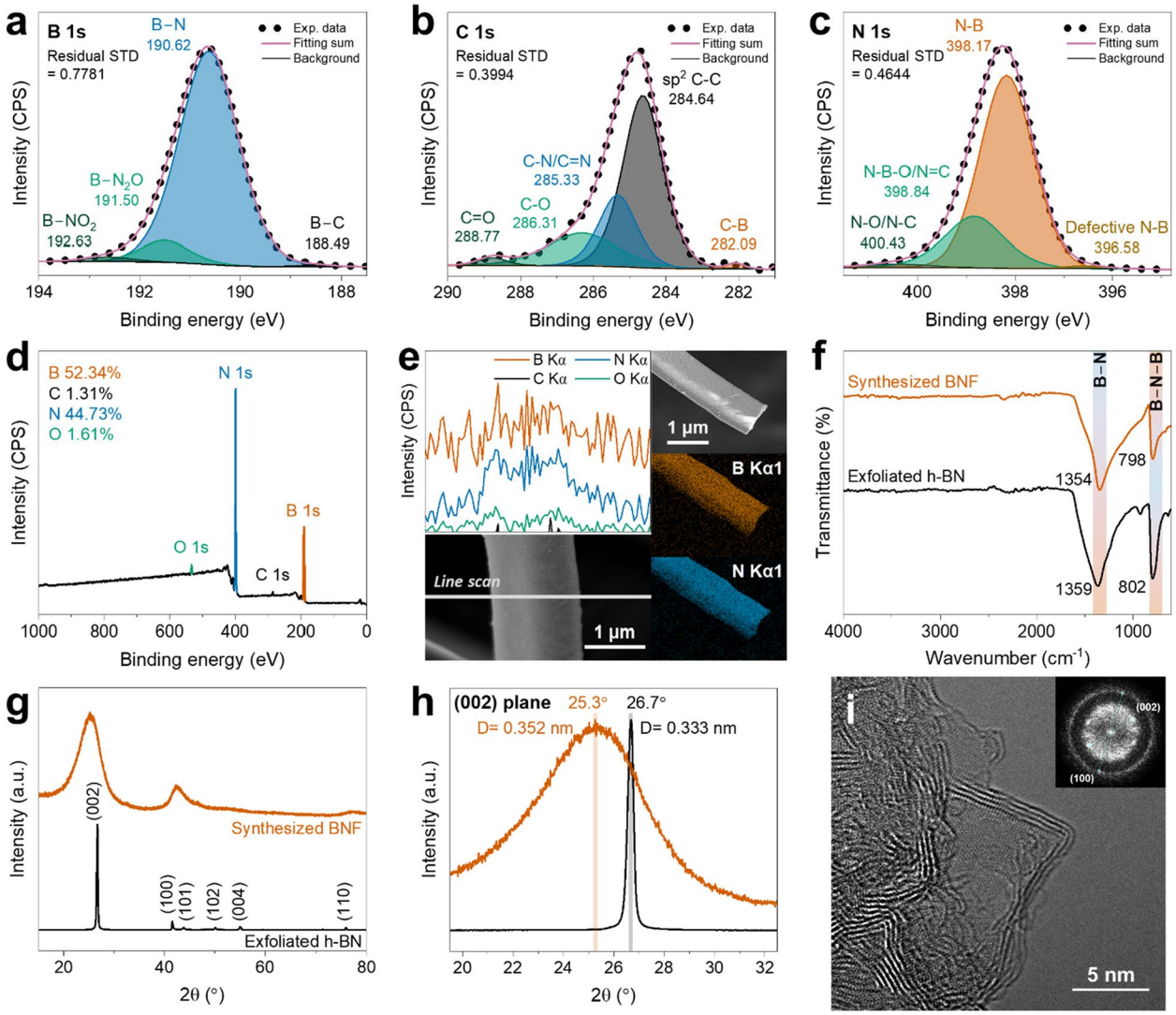

Fig. 5 Detailed characteristics of BNF. **a**–**c** High-resolution spectrum of **a** B 1 s, **b** C 1 s, and **c** N 1s. **d** XPS survey spectrum, inset shows calculated element content of B, C, N, and O. **e** EDX line scan profile and elementary mapping. **f** FT-IR spectra of synthesized BNF (orange) and exfoliated h-BN (black). **g**, **h** XRD pattern of synthesized BNF (orange) and exfoliated h-BN (black). **h** Enlarged (002) peak. **i** Typical TEM image of a BNF, inset shows the Fast Fourier Transform (FFT) of the image

compared to BNNS [75]. No additional peak between 3000 and 3500 cm^{-1} was observed for h-BN fibers.

The X-ray diffraction (XRD) pattern of the synthesized h-BN fibers also aligns with the pattern obtained from BNNS, displaying similar peak positions, and confirms the crystalline structure of h-BN fibers (BNF) (Fig. 5g, h). In the XRD spectrum, two broad peaks are observed at 2θ ~ 25° and 42°, corresponding to the (002) and (100) crystal planes of h-BN, respectively [76]. Compared with BNNS, the peaks show broadened width [FWHM: $BNF_{(002)}$ peak = 5.25° and $BNF_{(100)}$ peak = 2.65° *vs* $BNNS_{(002)}$ peak = 0.29° and $BNNS_{(100)}$ peak = 0.29°]. This is suggestive of a turbostratic structure of BN, with less extended/ordered stacking along both a- and c-axes. The calculated $d_{(002)}$ layer spacing for the h-BN fibers is 0.352 nm, slightly larger than that of BNNS (0.333 nm). This expansion is generally observed in 1D-structured BN materials due to the combination of turbostratic ordering and wall curvature. The crystallite size is calculated to be (002): 1.55 nm; (100): 3.22 nm; (101): 1.5 nm; (110): 2.83 nm (Figure S10). While the turbostratic polycrystalline structure is evident, the presence of higher resolved peaks, *e.g.*, (101), (102), (004), (110), in the XRD pattern of h-BN fibers indicates that a certain level of ordering is still present in the material.

High-resolution transmission electron microscopy (HRTEM) combined with fast Fourier transform patterning (FFT) was used to further quantify the degree of crystallinity of the synthesized h-BN fibers. The measured d-spacing is

0.334 nm for (002) planes and 0.214 nm for (100) planes, in agreement with previously reported values (Fig. 5i, Figure S11) [77]. FFT reveals the partially ordered structure, with ring-like diffraction patterns dominating that correspond to turbostratic or polycrystalline regions, in addition to several visible diffraction spots corresponding to hexagonal or crystalline regions [78]. These diffraction spots were assigned to the (002) and (100) planes, consistent with the results obtained from HRTEM and XRD analyses (Figure S12, S13). Combining both XRD and TEM data, we show the coexistence of t-BN and h-BN within the ceramic fibers. Such a structure is comparable to that observed in turbostratic graphite, where misalignment and d-spacing are revealed by XRD. In carbon-based materials, this does not imply the absence of crystalline regions, but rather a lack of consistent long-range order [79].

To give an indication of the mechanical properties of h-BN fibers, we have conducted nanoindentation of individual fibers on a single crystal silicon substrate. The elastic reduced modulus of h-BN fiber (1.1 ± 0.6 GPa) is in line with those observed in the BN nanotube fibers (~ 1.4 GPa) [8] and in the BN nanotube "buckypaper" (~ 1.2 GPa) [80]. The measured hardness in the h-BN fiber (11.1 ± 1.3 MPa) is also in line with the estimated tensile strength of the BN nanotube fibers (~ 15.7 MPa) [8] and the BN nanotube "buckypaper" (~ 13.8 MPa) [80] (see SI Figure S27 and S28 for detailed experimental measurements of the mechanical properties).

Overall, the detailed characterization of the annealed PMeABF demonstrates the fabrication of high-purity polycrystalline hexagonal/turbostratic form of h-BN fibers starting from a readily synthesized pre-ceramic B–N polymer precursor.

3 Conclusion

A straightforward method for the production of h-BN fibers is reported, that uses a combination of solution electrospinning and high-temperature annealing, using the well-defined polymer pre-ceramic, PMeAB. This air-stable, as a solid, main-chain B–N polymer is synthesized by a controlled atom-efficient catalytic dehydropolymerization of the readily available premonomer, $H_3B{\cdot}NMeH_2$, using very low loadings of catalysts that are commercially available (i.e., **[Ir]**). The degree of polymerization of PMeAB is readily controlled, and it can be synthesized on a 50 g scale. This straightforward synthesis of PMeAB, when combined with its non-volatility, high solubility, and high B–N content, makes it a promising single-source precursor for BN materials. To validate this hypothesis, examination of PMeAB's solution properties, electro-spinnability, and thermal behaviors, have been determined, for the first time, the optimal parameters for electrospinning PMeAB solutions into fibrous forms of PMeABF. Subsequent curing and high-temperature annealing using ammonolysis demonstrated the formation of cross-linked PMeABF and its gradual transition toward h-BN fibers with high purity and turbostratic ordering. To our knowledge, the method presented here represents the first instance of using an additive-free solution electrospinning process to produce h-BN fibers, highlighting the subsequent formation of stabilized PMeAB intermediates and ammonolysis-derived BN crystalline materials. Our route to h-BN fibers by electrospinning precisely controlled polyaminoborane pre-ceramic precursors offers advantages over the current state-of-the-art methods. It uses widely available, commercially accessible precursors and catalysts to straightforwardly generate PMeAB suitable for electrospinning and then h-BN fibers production. These practical improvements now allow for the development of larger scale manufacturing routes, which will allow for the exploration of these technologically important high-performance materials in a wide variety of settings such as fiber reinforced composites. Ongoing development efforts in the Grobert group include the implementation of needleless electrospinning, the use of rotary collectors, and the integration of precise flow-rate controllers, all aimed at enabling continuous, high-throughput production of BNF. The outcomes of these investigations will be reported in future work.

3.1 Materials and methods

3.1.1 Materials

Monomethylamineborane ($H_3B{\cdot}NMeH_2$) was purchased from *Boron Specialities LLC* (Ambridge, PA, USA). Chloroform ($CHCl_3$, 99 + %) was obtained from *Fisher Scientific*. Ammonia gas (NH_3, 99.98%) and argon gas (Ar, 99.998%) were purchased from *BOC*. All reagents were used without further purification unless otherwise specified.

Controlled catalytic synthesis of PMeAB A suitable vessel was charged with MeAB, then the THF solvent and catalyst (**[Rh]** [47], **[Ir]** [54], **[Ru]** [56], 0.01–0.1 mol% as a solid or as a THF solution) were then added. The flask was connected to an oil bubbler to vent the produced hydrogen gas, and the reaction stirred at 400 rpm, with the desired reaction temperature maintained via ice bath or recirculating chiller. In the case of dropwise addition, further MeAB as a solution in THF was added dropwise via syringe pump upon the initiation of catalysis. See Table S1 for further experimental details. After the completion of gas evolution, an in situ NMR sample (0.5 mL) was taken from the reaction mixture and analyzed by ^{1}H, $^{31}P\{^{1}H\}$ and ^{11}B NMR spectroscopies. Pentane was then added to the reaction mixture with rapid stirring to induce polymer precipitation. The white solid

PMeAB was isolated by filtration in-air, and the remaining volatiles were removed *in vacuo*. The obtained PMeAB was analyzed by ^{1}H and ^{11}B NMR spectroscopies along with GPC.

Electrospinning PMeAB fibers To prepare the spinning solutions, PMeAB with average molecular weights (M_w) ranging from 110,500 g·mol^{-1} to 290,500 g·mol^{-1} was dissolved in 2 mL of $CHCl_3$ of desired concentration. The dissolution process involved continuous stirring for 1 h at room temperature. Once the PMeAB was completely dissolved, the solution was transferred immediately to a 1 mL syringe equipped with a 23-gauge stainless steel needle. The syringe was connected to a high voltage supply (Genvolt High Voltage Power Supply). The solution was gravity-fed without the use of a syringe pump. The tip-to-collector distance was maintained at 30 cm throughout the electrospinning experiments. An applied voltage ranging from 20 to 35 kV was used to ensure optimal electrospinning continuity. The electrospinning process was conducted in a glove box with controlled temperature (20 ± 1 °C) and humidity ($15 \pm 1\%$). Finally, the PMeAB precursor fibers were collected on a piece of aluminium foil attached to a grounded metal substrate and could be easily peeled off into free-standing fibers mat.

Conversion of PMeAB fibers to BN fibers The conversion of PMeAB fibers to BN fibers involved two essential steps: curing and annealing. The curing process was carried out in a vacuum oven at a temperature of 100 °C for 48 h, maintaining a vacuum pressure below 10^{-1} bar. Subsequently, the cured PMeAB fibers were annealed in a high-temperature tube furnace. The fibers were heated directly to 1400 °C and held at that temperature for 2 h in an atmosphere consisting of a mixture of NH_3 and Ar gases in a volume ratio of 1:2. The samples were then allowed to cool naturally to room temperature. The heating rate from room temperature to 1400 °C was set at 10 °C/min.

Computational NMR studies All DFT calculations are performed with the Amsterdam Density Functional Package (ADF Version 2019.3) [81] The S12g functional [82] and ET-pVQZ basis set were used for geometry optimization, including COSMO solvation model and ZORA scalar relativistic corrections. Note that in all cases did we use the COSMO parameters for the solvent in which the experiments have been performed. NMR shielding constants were calculated at KT2 [83]/ET-pVQZ level using GIAO approach, following excellent results obtained in previous studies. The ET-pVQZ basis set is an even-tempered basis set of quadruple-z plus three polarization functions, which spans the whole range of diffuse and tight basis functions in a consistent manner. $BF_3{\cdot}Et_2O$ was taken as the reference compound for calculating the chemical shift and was treated in the same manner as the compounds to be evaluated. The chemical shift of the nucleus of interest (δ) is then given by.

$$\delta = \sigma_{iso}(reference) \; - \; \sigma_{iso}(nucleus\ of\ interest)$$

where σ_{iso}(reference) is the isotropic ^{11}B shielding constant of $BF_3{\cdot}Et_2O$ and σ_{iso}(nucleus of interest) the ^{11}B shielding constant of the nucleus of interest.

Characterization techniques All polymeric materials were analyzed by gel permeation chromatography (GPC) measured on a Malvern Viskotec GPC_{max} together with a Viskotec TDA 305 RI detector. Polymer M_n is referenced to polystyrene standards between M_n 474 and 476,800 g·mol^{-1}. All samples were passed through 3 columns consisting of a porous styrene divinylbenzene copolymer ($2 \times$ T5000 and $1 \times$ T4000 Malvern columns). The eluent used was GPC grade THF containing 0.1% w/w $[NBu_4]Br$ and the flow rate was 1 cm^3·min^{-1}. All polymer samples were dissolved in GPC grade THF $[NBu_4]Br$ (2 mg mL^{-1}) and filtered through a PTFE filter (pore size: 45 µm). The viscosity of the PMeAB solutions was measured using a Brookfield DV-II viscometer with a cone spindle CP-41. A fixed volume of 2 mL of the solution was loaded into the sample cup, and a ramping of rotation speed was employed from 50 to 120 rpm, corresponding to shear rates of $100-240$ s^{-1}. For highly viscous PMeAB solutions, the rotation speed was reduced to 10 rpm to maintain the % torque between 10 and 100%. The viscosity measurement was conducted twice, and the averaged viscosity values were reported. Surface tension measurements were performed using an Ossila contact angle goniometer in ambient conditions and calculated manually by combining Eqs. 1 and 2 proposed by Arashiro and Demarquette [84], and by referencing the table of H values provided by Andreas et al. [85] as a function of S, allowing γ to be determined from the photograph of a pendant drop.

$$\gamma = \frac{g \times D_e^2 \times \Delta\rho}{H} \tag{1}$$

where γ is the surface tension, g is the gravitational constant, Δρ is the density difference (in this case, the difference between the density of the polymer solution and the density of air, $\Delta\rho = \rho_{sol} - \rho_{air}$. Since $\rho_{sol} \gg \rho_{air}$, we approximate $\Delta\rho = \rho_{sol} - \rho_{air} \approx \rho_{sol}$), D_e is the equatorial diameter of the drop, H is a correction factor which is related to the shape factor of the pendant drop, S, defined as:

$$S = \frac{D_s}{D_e} \tag{2}$$

where D_s is the drop diameter measured horizontally at a distance D_e away from the apex of the drop.

Scanning electron microscopy (SEM) images were acquired using a Zeiss Merlin SEM and a JEOL JSM-840F SEM operating at an accelerating voltage of 3 kV. Prior to imaging, the samples were coated with a 10 nm layer of platinum (Pt). Fiber diameters were determined by analyzing at least 200 unbiased counts (major diameter of a dumbbell-like cross section) from the SEM images and fitting the resulting histogram. Energy-dispersive X-ray spectroscopy (EDX) line scanning and elemental mapping were performed using a Zeiss Merlin SEM operating at an accelerating voltage of 3 kV. Transmission electron microscopy (TEM) images were obtained using a JEOL JEM-2100F TEM operating at an acceleration voltage of 200 kV. X-ray Photoelectron Spectroscopy (XPS) analysis was conducted using a Thermo Scientific K-Alpha X-ray Photoelectron Spectrometer System. An ion pumped VG Microtech CLAM 4 MCD analyzer system equipped with unmonochromated Mg K_α X-ray radiation of 1253.6 eV was used. Fourier transform infrared (FT-IR) spectroscopy attenuated total reflection (ATR) spectra were recorded using a Varian Excalibur FTS 3500 FT-IR spectrometer in the range of 600 to 4000 cm^{-1}. X-ray diffraction (XRD) analysis was performed at room temperature using a Siemens D5000 powder diffractometer with copper Kα radiation ($\lambda = 0.15406$ nm) and a secondary monochromator. The samples were continuously rotated During data collection, and a step size of 0.05° 2θ was used in the range of 10–100° 2θ with a count time of 12 s per step. Thermogravimetric Analyser with Mass Spectrometer (TGA–DSC-MS) measurements were conducted using a STA 449 F3 Jupiter® instrument coupled with a 403 Aëolos Quadro quadrupole mass spectrometer. The samples were heated in Ar atmosphere from room temperature to 1400 °C at a heating rate of 10 °C/min. The quadrupole was used to scan all m/z ratios from m/z = 1 to m/z = 150 approximately every 30 s. ^{11}B magic angle spinning – nuclear magnetic resonance (^{11}BMAS-NMR) measurements were carried out at 128.39 MHz using a Varian VNMRS spectrometer and 4 mm (rotor o.d.) probe. Spectra were acquired at a spin rate of 12 kHz. All direct excitation ^{11}B spectra were acquired with a 1 µs 30° solid pulse, which was determined from a 6 µs solution pulse determined on $BF_3{\cdot}OEt_2$. The spectra were acquired with a recycle delay of 1 s determined on the sample. Boron spectral referencing is relative to $BF_3{\cdot}OEt_2$. Nanoindentation tests were conducted with a standard Berkovich diamond tip using a low load module on a Hysitron TI Premier. The tip shape was calibrated using fused silica, and the hardness and reduced modulus measurements from the samples were calculated using the formulars introduced by Oliver and Pharr [86]. Precursor PMeAB fibers were directly electrospun onto single crystal silicon wafers, and BN fibers were dissolved in acetone and drop-cast onto single crystal silicon wafers prior to the measurements.

Supplementary information The online version contains supplementary material available at https://doi.org/10.1007/s42114-025-01418-7.

Acknowledgements We thank Greg Cook and Richard Turner for their technical support. We also acknowledge the microscopy and spectrometry support from the Oxford Materials Characterization Service and the David Cockayne Centre for Electron Microscopy, Department of Materials, University of Oxford, Dr Alexander Watson for useful discussions, and Niall Donaldson for ICP-OES analysis. Additional support was provided by the Henry Royce Institute (EP/R010145/1). NG thanks The Royal Society for the Royal Society Industry Fellowship.

Author contributions All authors contributed to the study conception and design. MC, CVB, and CNB conducted the synthesis of PMeAB under the supervision of ASW. PL conducted processing and characterization of PMeAB fibers and BN fibers and GTT conducted HRTEM under the supervision of BMM and NG. RMS conducted STEM imaging under the supervision of NG. SP performed the solid-state 11B NMR measurement. All authors read and approved the final manuscript. PL and BMM contributed equally to this work.

Funding This work was financially supported by the Faraday Institution (BMM, NG), the EPSRC EP/R00661X/1 (BMM, NG), The Royal Society- RSIF IF160009 (NG), EP/T5171811/1 (GTT, RMS), EP/M024210/2 (ASW), the University of York IAA fund (ASW), the University of York (CVB, MC), AEI/MCIU (PID2020-114548GB-I00, PID2023-152415NB-I00), GenCat (2021SGR00487) a developer's license by SCM (MS), and the University of Girona (IFUdG 68 2022).

Data availability No datasets were generated or analysed during the current study.

Declarations

Competing interests This work has resulted in two patents (GB2416470.9 and GB2416458.4) which were filed on 8 November 2024.

References

1. Ince JC, Peerzada M, Mathews LD, Pai AR, Al-qatatsheh A, Abbasi S, Yin Y, Hameed N, Duffy AR, Lau AK, Salim NV (2023) Overview of emerging hybrid and composite materials for space applications. Adv Compos Hybrid Mater 6(4):130. https://doi.org/10.1007/s42114-023-00678-5
2. Chen Y, Zhang J, Li Z, Zhang H, Chen J, Yang W, Yu T, Liu W, Li Y (2023) Manufacturing technology of lightweight fiber-reinforced composite structures in aerospace: current situation

and toward intellectualization. Aerospace. https://doi.org/10.3390/aerospace10030206
3. Zhang W, Xu J (2022) Advanced lightweight materials for automobiles: a review. Mater Des 221:110994
4. Economy J, Lin R (1977) Boron nitride fibers. In Boron and refractory borides; Matkovich VI (ed); Springer Berlin Heidelberg: Berlin, Heidelberg, pp 552–564. https://doi.org/10.1007/978-3-642-66620-9_29
5. Kostoglou N, Polychronopoulou K, Rebholz C (2015) Thermal and chemical stability of hexagonal boron nitride (h-BN) nanoplatelets. Vacuum 112:42–45. https://doi.org/10.1016/j.vacuum.2014.11.009
6. Falin A, Cai Q, Santos EJG, Scullion D, Qian D, Zhang R, Yang Z, Huang S, Watanabe K, Taniguchi T, Barnett MR, Chen Y, Ruoff RS, Li LH (2017) Mechanical properties of atomically thin boron nitride and the role of interlayer interactions. Nat Commun 8(1):15815. https://doi.org/10.1038/ncomms15815
7. Jones RS, Gonzalez-Munoz S, Griffiths I, Holdway P, Evers K, Luanwuthi S, Maciejewska BM, Kolosov O, Grobert N (2023) Thermal conductivity of carbon/boron nitride heteronanotube and boron nitride nanotube buckypapers: implications for thermal management composites. ACS Appl Nano Mater 6(17):15374–15384. https://doi.org/10.1021/acsanm.3c01147
8. Simonsen Ginestra CJ, Martínez-Jiménez C, Matatyaho Ya'akobi A, Dewey OS, Smith McWilliams AD, Headrick RJ, Acapulco JA, Scammell LR, Smith MW, Kosynkin DV, Marincel DM, Park C, Chu SH, Talmon Y, Martí AA, Pasquali M (2022) Liquid crystals of neat boron nitride nanotubes and their assembly into ordered macroscopic materials. Nat Commun 13(1):3136. https://doi.org/10.1038/s41467-022-30378-5.
9. Chen J, Huang X, Sun B, Jiang P (2019) Highly thermally conductive yet electrically insulating polymer/boron nitride nanosheets nanocomposite films for improved thermal management capability. ACS Nano 13(1):337–345. https://doi.org/10.1021/acsnano.8b06290
10. Toury B, Miele P, Cornu D, Vincent H, Bouix J (2002) Boron nitride fibers prepared from symmetric and asymmetric alkylaminoborazines. Adv Funct Mater 12(3):228–234
11. Bernard S, Miele P (2014) Polymer-derived boron nitride: a review on the chemistry, shaping and ceramic conversion of borazine derivatives. Materials 7(11):7436–7459. https://doi.org/10.3390/ma7117436
12. Kimura Y, Kubo Y, Hayashi N (1994) High-performance boron-nitride fibers from poly(borazine) preceramics. Compos Sci Technol 51(2):173–179
13. Guilhon F, Bonnetot B, Cornu D, Mongeot H (1996) Conversion of tris(isopropylamino)borane to polyborazines. Thermal degradation to boron nitride. Polyhedron 15(5):851–859. https://doi.org/10.1016/0277-5387(95)00336-6
14. Hwang HJ, Barakat NAM, Kanjwal MA, Sheikh FA, Kim HY, Abadir MF (2010) Boron nitride nanofibers by the electrospinning technique. Macromol Res 18(6):551–557. https://doi.org/10.1007/s13233-010-0601-2
15. Qiu Y, Yu J, Rafique J, Yin J, Bai X, Wang E (2009) Large-scale production of aligned long boron nitride nanofibers by multijet/multicollector electrospinning. J Phys Chem C Nanomater Interfaces 113(26):11228–11234. https://doi.org/10.1021/jp901267k
16. Qiu Y, Yu J, Yin J, Tan C, Zhou X, Bai X, Wang E (2009) Synthesis of continuous boron nitride nanofibers by solution coating electrospun template. Nanotechnology 20(34):345603. https://doi.org/10.1088/0957-4484/20/34/345603
17. Salles V, Bernard S, Brioude A, Cornu D, Miele P (2010) A new class of boron nitride fibers with tunable properties by combining an electrospinning process and the polymer-derived ceramics route. Nanoscale 2(2):215–217. https://doi.org/10.1039/B9NR00185A
18. Toury B, Bernard S, Cornu D, Chassagneux F, Létoffé JM, Miele P (2003) High-performance boron nitride fibers obtained from asymmetric alkylaminoborazine. J Mater Chem 13(2):274–279. https://doi.org/10.1039/b207476a
19. Kim JH, Pham TV, Hwang JH, Kim CS, Kim MJ (2018) Boron nitride nanotubes: synthesis and applications. Nano Convergence 5(1):17. https://doi.org/10.1186/s40580-018-0149-y
20. Jones RS (2021) Designing boron nitride nanotubes and their macroscopic assemblies via sacrificial templating. PhD thesis, University of Oxford, Oxford. https://solo.bodleian.ox.ac.uk/permalink/44OXF_INST/35n82s/alma991025215667807026
21. Diana Santiago; Maricela Lizcano; Thomas Sabo (2020) Fabrication of boron nitride fibers by force spinning method. https://ntrs.nasa.gov/citations/20200001018.
22. Vailonis K, Santiago D, Lizcano M, Sabo T, Roy A (2023) Forcespun polymers as precursors to boron nitride fibers. Document ID: 20230011556, Glenn Research Centre American Association for Advances in Functional Materials Conference. https://ntrs.nasa.gov/citations/20230011556. Accessed Aug 2023
23. Bernard S, Salameh C, Miele P (2016) Boron nitride ceramics from molecular precursors: synthesis, properties and applications. Dalton Trans 45(3):861–873. https://doi.org/10.1039/C5DT03633J
24. Lindquist DA, Janik JF, Datye AK, Paine RT, Rothman JB (1992) Boron nitride fibers processed from poly(borazinylamine) solutions. Chem Mater 4(1):17–19. https://doi.org/10.1021/cm00019a007
25. Cornu D, Bernard S, Duperrier S, Toury B, Miele P (2005) Alkylaminoborazine-based precursors for the preparation of boron nitride fibers by the polymer-derived ceramics (PDCs) route. J Eur Ceram Soc 25(2):111–121
26. Duperrier S, Gervais C, Bernard S, Cornu D, Babonneau F, Balan C, Miele P (2007) Design of a series of preceramic B-tri(methylamino)borazine-based polymers as fiber precursors: architecture, thermal behavior, and melt-spinnability. Macromolecules 40(4):1018–1027. https://doi.org/10.1021/ma0623035
27. Marchionni D, Basak S, Khodadadi AN, Marrocchi A, Vaccaro L (2023) Synthesis and applications of organic borazine materials. Adv Funct Mater 33(49):2303635. https://doi.org/10.1002/adfm.202303635
28. Fazen PJ, Remsen EE, Beck JS, Carroll PJ, McGhie AR, Sneddon LG (1995) Synthesis, properties, and ceramic conversion reactions of polyborazylene. A high-yield polymeric precursor to boron nitride. Chem Mater 7(10):1942–1956. https://doi.org/10.1021/cm00058a028
29. Wu C, Wang B, Wu N, Han C, Zhang X, Shen S, Tian Q, Qin C, Li P, Wang Y (2020) Molecular-scale understanding on the structure evolution from melamine diborate supramolecule to boron nitride fibers. Ceram Int 46(1):1083–1090. https://doi.org/10.1016/j.ceramint.2019.09.075
30. Du Y, Wang B, Li W, Song Q, Shao C, Han C, Wang Y (2021) Design and synthesis of a novel spinnable polyborazine precursor with high ceramic yield via one-pot copolymerization. J Am Ceram Soc 104(11):5509–5520
31. Mohajeri N, T-Raissi A (2006) Regeneration of ammonia-borane complex for hydrogen storage. MRS Online Proceedings Library 884(1):14. https://doi.org/10.1557/PROC-884-GG1.4
32. Dong S, Maciejewska BM, Lißner M, Thomson D, Townsend D, Millar R, Petrinic N, Grobert N (2023) Unveiling the mechanism of the in situ formation of 3D fiber macroassemblies with controlled properties. ACS Nano 17(7):6800–6810. https://doi.org/10.1021/acsnano.3c00289
33. Schofield RM, Maciejewska BM, Dong S, Tebbutt GT, McGurty D, Bonilla RS, Assender HE, Grobert N (2023) Driving fiber diameters to the limit: nanoparticle-induced diameter reductions in electrospun photoactive composite nanofibers for organic

photovoltaics. Adv Compos Hybrid Mater 6(6):229. https://doi.org/10.1007/s42114-023-00788-0
34. Dong S, Maciejewska BM, Lißner M, Thomson D, Townsend D, Millar R, Petrinic N, Grobert N (2023) Unveiling the mechanism of the *in situ* formation of 3D fiber macroassemblies with controlled properties. ACS Nano. https://doi.org/10.1021/acsnano.3c00289
35. Vidal F, Jäkle F (2019) Functional polymeric materials based on main-group elements. Angew Chem Int Ed Engl 58(18):5846–5870. https://doi.org/10.1002/anie.201810611
36. Ryan DE, Andrea KA, Race JJ, Boyd TM, Lloyd-Jones GC, Weller AS (2020) Amine–borane dehydropolymerization using Rh-based precatalysts: resting state, chain control, and efficient polymer synthesis. ACS Catal 10(14):7443–7448. https://doi.org/10.1021/acscatal.0c02211
37. Han D, Anke F, Trose M, Beweries T (2019) Recent advances in transition metal catalysed dehydropolymerisation of amine boranes and phosphine boranes. Coord Chem Rev 380:260–286
38. De Albuquerque Pinheiro CA, Roiland C, Jehan P, Alcaraz G (2018) Solventless and metal-free synthesis of high-molecular-mass polyaminoboranes from diisopropylaminoborane and primary amines. Angew Chem Int Ed 57(6):1519–1522. https://doi.org/10.1002/anie.201710293
39. Devillard M, De Albuquerque Pinheiro CA, Caytan E, Roiland C, Dinoi C, Del Rosal I, Alcaraz G (2021) Uncatalyzed formation of polyaminoboranes from diisopropylaminoborane and primary amines: a kinetically controlled polymerization reaction. Adv Synth Catal 363(9):2417–2426. https://doi.org/10.1002/adsc.202001458
40. Staubitz A, Presa Soto A, Manners I (2008) Iridium-catalyzed dehydrocoupling of primary amine–borane adducts: a route to high molecular weight polyaminoboranes, boron–nitrogen analogues of polyolefins. Angewandte Chemie Int Edition 47(33):6212–6215. https://doi.org/10.1002/anie.200801197
41. Staubitz A, Sloan ME, Robertson APM, Friedrich A, Schneider S, Gates PJ, Schmedt auf der Günne J, Manners I (2010) Catalytic dehydrocoupling/dehydrogenation of N-methylamine-borane and ammonia-borane: synthesis and characterization of high molecular weight polyaminoboranes. J Am Chem Soc 132(38):13332–13345. https://doi.org/10.1021/ja104607y
42. Stubbs NE, Jurca T, Leitao EM, Woodall CH, Manners I (2013) Polyaminoborane main chain scission using N-heterocyclic carbenes; formation of donor-stabilised monomeric aminoboranes. Chem Commun 49(80):9098–9100. https://doi.org/10.1039/C3CC44373F
43. Leitao EM, Jurca T, Manners I (2013) Catalysis in service of main group chemistry offers a versatile approach to P-block molecules and materials. Nat Chem 5(10):817–829. https://doi.org/10.1038/nchem.1749
44. Kim DP, Moon KT, Kho JG, Economy J, Gervais C, Babonneau F (1999) Synthesis and characterization of poly(aminoborane) as a new boron nitride precursor. Polym Adv Technol 10(12):702–712. https://doi.org/10.1002/(SICI)1099-1581(199912)10:12<702::AID-PAT931>3.0.CO;2-Q
45. Bowden ME, Brown IWM, Gainsford GJ, Wong H (2008) Structure and thermal decomposition of methylamine borane. Inorg Chim Acta 361(7):2147–2153. https://doi.org/10.1016/j.ica.2007.10.034
46. Chen EY-X (2009) Coordination polymerization of polar vinyl monomers by single-site metal catalysts. Chem Rev 109(11):5157–5214. https://doi.org/10.1021/cr9000258
47. Brodie NC, Boyd TM, Sotorríos L, Ryan DE, Magee E, Huband S, Town JS, Lloyd-Jones GC, Haddleton DM, Macgregor SA, Weller AS (2021) Controlled synthesis of well-defined polyaminoboranes on scale using a robust and efficient catalyst. J Am Chem Soc 143(49):21010–21023. https://doi.org/10.1021/jacs.1c10888
48. Jurca T, Dellermann T, Stubbs NE, Resendiz-Lara DA, Whittell GR, Manners I (2018) Step-growth titanium-catalysed dehydropolymerisation of amine–boranes. Chem Sci 9(13):3360–3366. https://doi.org/10.1039/C7SC05395A
49. Peterson GI, Choi T-L (2020) Cascade polymerizations: recent developments in the formation of polymer repeat units by cascade reactions. Chem Sci 11(19):4843–4854. https://doi.org/10.1039/D0SC01475C
50. Metters OJ, Chapman AM, Robertson APM, Woodall CH, Gates PJ, Wass DF, Manners I (2014) Generation of aminoborane monomers RR'N=BH_2 from amine-boronium cations [RR'NH-BH_2L](+): metal catalyst-free formation of polyaminoboranes at ambient temperature. Chem Commun (Camb) 50(81):12146–12149. https://doi.org/10.1039/c4cc05145a
51. Bhunya S, Malakar T, Paul A (2014) Unfolding the crucial role of a nucleophile in Ziegler-Natta type Ir catalyzed polyaminoborane formation. Chem Commun 50(44):5919–5922. https://doi.org/10.1039/C4CC01337A
52. Ravve A (2012) In: Principles of polymer chemistry. Ravve A (ed), Springer New York, New York, NY. https://doi.org/10.1007/978-1-4614-2212-9_7
53. Potter RG, Camaioni DM, Vasiliu M, Dixon DA (2010) Thermochemistry of Lewis adducts of BH_3 and nucleophilic substitution of triethylamine on NH_3BH_3 in tetrahydrofuran. Inorg Chem 49(22):10512–10521. https://doi.org/10.1021/ic101481c
54. Göttker-Schnetmann I, White PS, Brookhart M (2004) Synthesis and properties of iridium bis(phosphinite) pincer complexes (p-XPCP)IrH_2, (p-XPCP)Ir(CO), (p-XPCP)Ir(H)(Aryl), and {(p-XPCP)Ir}$_2${μ-N_2} and their relevance in alkane transfer dehydrogenation. Organometallics 23(8):1766–1776. https://doi.org/10.1021/om030670o
55. Blaquiere N, Diallo-Garcia S, Gorelsky SI, Black DA, Fagnou K (2008) Ruthenium-catalyzed dehydrogenation of ammonia boranes. J Am Chem Soc 130(43):14034–14035. https://doi.org/10.1021/ja804235t
56. Cross MJ, Sajjad MA, Macgregor SA, Weller AS (2025) Square planar Ru($Pr_2PCH_2CH_2NH$)$_2$ and its role in fast and selective catalytic amine–borane dehydropolymerization to form high molecular weight polyaminoboranes. Angew Chem Int Ed. https://doi.org/10.1002/anie.202500019
57. Glüer A, Förster M, Celinski VR, Schmedt auf der Günne J, Holthausen MC, Schneider S (2015) Highly active iron catalyst for ammonia borane dehydrocoupling at room temperature. ACS Catal 5(12):7214–7217. https://doi.org/10.1021/acscatal.5b02406.
58. Shenoy SL, Bates WD, Frisch HL, Wnek GE (2005) Role of chain entanglements on fiber formation during electrospinning of polymer solutions: good solvent, non-specific polymer-polymer interaction limit. Polymer (Guildf) 46(10):3372–3384. https://doi.org/10.1016/j.polymer.2005.03.011
59. Lahann J (2010) Science and technology of polymer nanofibers. Macromol Chem Phys 211(12):1387–1387. https://doi.org/10.1002/macp.201000211
60. Okutan N, Terzi P, Altay F (2014) Affecting parameters on electrospinning process and characterization of electrospun gelatin nanofibers. Food Hydrocolloids 39:19–26. https://doi.org/10.1016/j.foodhyd.2013.12.022
61. Amariei N, Manea LR, Bertea AP, Bertea A, Popa A (2017) The influence of polymer solution on the properties of electrospun 3D nanostructures. IOP Conf Ser Mater Sci Eng 209(1):012092. https://doi.org/10.1088/1757-899X/209/1/012092
62. Xue J, Wu T, Dai Y, Xia Y (2019) Electrospinning and electrospun nanofibers: methods, materials, and applications. Chem Rev. https://doi.org/10.1021/acs.chemrev.8b00593
63. Koski A, Yim K, Shivkumar S (2004) Effect of molecular weight on fibrous PVA produced by electrospinning. Mater Lett 58(3–4):493–497. https://doi.org/10.1016/S0167-577X(03)00532-9

64. Han D, Joksch M, Klahn M, Spannenberg A, Drexler H-J, Baumann W, Jiao H, Knitsch R, Hansen MR, Eckert H, Beweries T (2016) Iridium(Iii) hydrido complexes for the catalytic dehydrogenation of hydrazine borane. Dalton Trans 45(44):17697–17704. https://doi.org/10.1039/C6DT03068H
65. Knitsch R, Han D, Anke F, Ibing L, Jiao H, Hansen MR, Beweries T (2019) Fe(II) hydride complexes for the homogeneous dehydrocoupling of hydrazine borane: catalytic mechanism via DFT calculations and detailed spectroscopic characterization. Organometallics 38(14):2714–2723. https://doi.org/10.1021/acs.organomet.9b00053
66. Wang X, Zhi C, Li L, Zeng H, Li C, Mitome M, Golberg D, Bando Y (2011) "Chemical blowing" of thin-walled bubbles: high-throughput fabrication of large-area, few-layered BN and Cx-BN nanosheets. Adv Mater 23(35):4072–4076. https://doi.org/10.1002/adma.201101788
67. Chrenko RM (1974) Ultraviolet and infrared spectra of cubic boron nitride. Solid State Commun 14(6):511–515
68. Duperrier S, Gervais C, Bernard S, Cornu D, Babonneau F, Miele P (2006) Controlling the chemistry, morphology and structure of boron nitride-based ceramic fibers through a comprehensive mechanistic study of the reactivity of spinnable polymers with ammonia. J Mater Chem 16(30):3126–3138. https://doi.org/10.1039/B604482D
69. Lei Y, Wang Y, Song Y (2012) Boron nitride by pyrolysis of the melt-processable poly[tris(methylamino)borane]: structure, composition and oxidation resistance. Ceram Int 38(1):271–276
70. Lei Y, Wang Y, Song Y, Deng C, Wang H (2011) Nearly stoichiometric BN fiber by curing and thermolysis of a novel poly[(alkylamino)borazine]. Ceram Int 37(6):1795–1800. https://doi.org/10.1016/j.ceramint.2011.03.007
71. Zhang C, Zhao S, Jin C, Koh AL, Zhou Y, Xu W, Li Q, Xiong Q, Peng H, Liu Z (2015) Direct growth of large-area graphene and boron nitride heterostructures by a co-segregation method. Nat Commun 6(1):6519. https://doi.org/10.1038/ncomms7519
72. Pang J, Chao Y, Chang H, Li H, Xiong J, He M, Zhang Q, Li H, Zhu W (2017) Tuning electronic properties of boron nitride nanoplate via doping carbon for enhanced adsorptive performance. J Colloid Interface Sci 508:121–128
73. Tay RY, Li H, Tsang SH, Jing L, Tan D, Wei M, Teo EHT (2015) Facile synthesis of millimeter-scale vertically aligned boron nitride nanotube forests by template-assisted chemical vapor deposition. Chem Mater 27(20):7156–7163. https://doi.org/10.1021/acs.chemmater.5b03300
74. Fan D, Feng J, Liu J, Gao T, Ye Z, Chen M, Lv X (2016) Hexagonal boron nitride nanosheets exfoliated by sodium hypochlorite ball mill and their potential application in catalysis. Ceram Int 42(6):7155–7163. https://doi.org/10.1016/j.ceramint.2016.01.105
75. Du M, Wu Y, Hao X (2013) A facile chemical exfoliation method to obtain large size boron nitride nanosheets. CrystEngComm 15(9):1782–1786. https://doi.org/10.1039/C2CE26446C
76. Kurakevych OO, Solozhenko VL (2007) Rhombohedral boron subnitride, B 13N 2, by X-Ray Powder Diffraction. Acta Crystallogr C 63(9):i80–i82. https://doi.org/10.1107/S0108270107037353
77. Xue Y, Zhou X, Zhan T, Jiang B, Guo Q, Fu X, Shimamura K, Xu Y, Mori T, Dai P, Bando Y, Tang C, Golberg D (2018) Densely interconnected porous BN frameworks for multifunctional and isotropically thermoconductive polymer composites. Adv Funct Mater. https://doi.org/10.1002/adfm.201801205
78. Maleki M, Beitollahi A, Shokouhimehr M (2015) Template-free synthesis of porous boron nitride using a single source precursor. RSC Adv 5(58):46823–46828. https://doi.org/10.1039/c5ra04636j
79. Monthioux M (2024) Describing carbons. Carbon Trends. https://doi.org/10.1016/j.cartre.2024.100325
80. Nautiyal P, Zhang C, Loganathan A, Boesl B, Agarwal A (2019) High-temperature mechanics of boron nitride nanotube "buckypaper" for engineering advanced structural materials. ACS Appl Nano Mater 2(7):4402–4416. https://doi.org/10.1021/acsanm.9b00817
81. te Velde G, Bickelhaupt FM, Baerends EJ, Fonseca Guerra C, van Gisbergen SJA, Snijders JG, Ziegler T (2001) Chemistry with ADF. J Comput Chem 22(9):931–967
82. Swart M (2013) A new family of hybrid density functionals. Chem Phys Lett 580:166–171
83. Keal TW, Tozer DJ (2004) A semiempirical generalized gradient approximation exchange-correlation functional. J Chem Phys 121(12):5654–5660. https://doi.org/10.1063/1.1784777
84. Arashiro EY, Demarquette NR (1999) Use of the pendant drop method to measure interfacial tension between molten polymers. Mater Res 2:23–32
85. Andreas JM, Hauser EA, Tucker WB (1938) Boundary tension by pendant drops[1]. J Phys Chem 42(8):1001–1019. https://doi.org/10.1021/j100903a002
86. Oliver WC, Pharr GM (2004) Measurement of hardness and elastic modulus by instrumented indentation: advances in understanding and refinements to methodology. J Mater Res 19(1):3–20. https://doi.org/10.1557/jmr.2004.19.1.3